Nanoscale Advances

Accepted Manuscript

This article can be cited before page numbers have been issued, to do this please use: B. Boruah, R. Gupta, J. Modak and G. Madras, *Nanoscale Adv.*, 2019, DOI: 10.1039/C9NA00305C.

ROYAL SOCIETY OF CHEMISTRY

rsc.li/nanoscale-advances

View Article Online
DOI: 10.1039/C9NA00305C

Enhanced Photocatalysis and Bacterio-inhibition in Nb_2O_5 via Versatile Doping of Metal (Sr, Y, Zr, Ag): A Critical assessment

*Bhanupriya Boruah, Rimzhim Gupta, Jayant M Modak, Giridhar Madras**

Department of Chemical Engineering,

Indian Institute of Science,

Bangalore 560012. India.

* Corresponding author. Tel. +91 80 22932321; Fax: +91 80 23600683,
E-mail: giridhar@chemeng.iisc.ernet.in (G. Madras)

Abstract

Unique optical properties render the semiconductor Nb_2O_5 nanoparticles suitable for light harvesting and photocatalytic applications. This study focuses on determining the optical properties such as band gap, conduction band edge, valence band edge and the work function of as-prepared solution combustion synthesized Nb_2O_5 nanoparticles with the help of UV-Vis Diffused Reflectance spectroscopy (DRS) and Ultraviolet photoelectron spectroscopy (UPS) techniques. Phase purity and the oxidation states of the elements present in the material were confirmed from X-ray Diffraction (XRD) patterns and X-ray photoelectron spectroscopy (XPS), respectively. Doping semiconductors with different metal ions impact the activity of the material, and therefore efforts were made to understand the effect on the photocatalytic performance of Nb_2O_5 due to the incorporation of metal dopants viz Sr, Y, Zr, and Ag. Lattice parameters were obtained from Rietveld refinement of the XRD patterns. Parameters which are closely related to the photoactivity of the catalysts such as presence of surface defects, oxygen vacancies, surface area, charge carrier dynamics were determined from Photoluminescence (PL) analysis, Brunauer Emmett Teller (BET) surface area measurements and Time-resolved fluorescence (TRF) analysis respectively. In addition the dopant concentrations were optimised for enhanced photocatalytic activity. The doped Nb_2O_5 nanoparticles showed significant activity towards targeted degradation of organic pollutants like 2-chlorophenol (2-CP) and dye contaminants like methylene blue (MB), orange G (OG) and indigo carmine (IC). This strategy yielded a robust response towards inactivation of *E.coli* and *S.aureus* as well. Adsorption and photodegradation of MB followed Lagergren's pseudo 1st order reaction model and Langmuir Hinshelwood model respectively. Bacteria inactivation and OG, IC and 2-CP photodegradation followed 1st order kinetics. Reusability of the catalyst for 5 cycles was demonstrated. Finally, a plausible mechanism is

DOI: 10.1039/C9NA00305C

proposed based on radical trapping experiments and combined analysis of the characterization techniques.

Keywords: Nb_2O_5; metal dopants; photocatalysis; *E. coli* inactivation; dye degradation, chlorophenol degradation

1 Introduction

Water pollution from industrial discharges is a major global concern and tackling such problems require effective environment-friendly water treatment technology.[1] Dyes are a kind of pollutants produced from textile, paint, paper, food, and leather industries. About 280,000 tons of dyes are discharged every year into the aquatic system [2]. Chlorophenols represent another class of water pollutants, which are considered as toxic to humans by US EPA, are mainly produced from petroleum and pesticide manufacturing industries [3]. Apart from these pollutants, water contaminated from coliform bacteria also poses serious health threats [4, 5] . To address these issues, conventional water treatment methods such as adsorption [6], coagulation [7], filtration [8], ion exchange [9] are found to be effective but they lead to the generation of secondary pollutants. Traditional disinfection methods such as using UV light is costly [10, 11] and chlorination generate harmful by-products [12, 13]. Advanced oxidation processes (AOP) have been used as an alternative for wastewater treatment since the 1990s. Among AOP's, heterogeneous photocatalysis has shown great potential in disinfecting water and degrading chemical contaminants [14].

Photocatalysis involves the usage of semiconductors that function as a catalyst on exposure to irradiation. The photogenerated charge carriers from the semiconductor produce reactive oxygen species to carry out the photodegradation of pollutants [15]. TiO_2 and ZnO are regarded as efficient photocatalysts for water decontamination [16, 17] and have a band gap of around 3-3.2 eV [18-20]. The similar band gap is observed in Nb_2O_5 which is an n-type semiconductor [21]. It is broadly utilized in the field of gas sensing [22], glass manufacturing [23], electrochemical energy storage applications [24] but limited reports are available on Nb_2O_5 as a photocatalyst and its related photochemical properties [21, 25, 26]. As Nb_2O_5 exhibits similar semi conducting property as that of TiO_2, this material has great potential to replace the widely studied titania.

View Article Online
DOI: 10.1039/C9NA00305C

The efficiency of photocatalyzed reactions can reduce due to charge carrier recombination. This can be avoided by doping the semiconductor with metals or non-metal impurities [27]. The dopants should serve as the trapping sites for electron or hole to increase the activity of the photocatalyst [28]. Doping leads to the creation of local energy states in the forbidden gap and could also narrow the band gap [29]. Additionally, dopant incorporation could change the particle size, specific surface area, morphology of the nanoparticles which impacts the photoactivity [30]. Sood et al. found that Sr^{2+} doping enhanced the photocatalytic activity of TiO_2 towards brilliant green degradation due to an increase in the surface area and delay in the recombination time of excitons [31]. Similar changes in the properties of TiO_2 due to the incorporation of Y^{3+} dopant was observed and the doped material showed excellent activity towards MO photodegradation [32]. Silver doping in TiO_2 was found to red shift the absorption range and enhance the separation efficiency of electron-hole, thus showing good photocatalytic activity in the visible region towards Cr (VI) reduction [33]. Incorporation of Zr^{4+} in TiO_2 resulted in lattice defects and showed higher photoactivity towards the degradation of rhodamine B [34]. Extensive studies were performed on TiO_2 doped systems but the literature contains few efforts on the photoelectrochemical properties of doped Nb_2O_5 systems and its related application. Nb_2O_5 doped with Eu^{3+} exhibited strong emission at 610 nm with long decay times making it suitable for lighting devices [35]. Esteves et al. studied the effect of Mo and W doped Nb_2O_5 for the photooxidation of organic pollutants [36].

In view of the captivating features of doped systems, we have initially studied the changes in physical and chemical properties of solution combustion synthesized Nb_2O_5 due to incorporation of metals dopants viz. Sr, Y, Zr, and Ag using characterization techniques such as XRD, XPS, SEM, TEM, BET surface area measurements. We have especially emphasized on analysing the optical properties of pristine and metal-doped Nb_2O_5 such as narrowing of the band gap, band edge details, presence of defects and charge carrier dynamics using DRS,

View Article Online
DOI: 10.1039/C9NA00305C

UPS, PL, and TRF spectroscopy techniques. From the above analyses, optimized concentration of these dopants in Nb_2O_5 was concluded and later validated it experimentally from MB photodegradation. Next, we have checked the photoactivity of these materials over a wide range of water pollutants. To the best of our knowledge, this is the first time the effect of Sr, Y, Zr, and Ag doped Nb_2O_5 has been observed for the photocatalytic degradation of various dyes, organics as well as for the inactivation of bacteria. Further, kinetic studies for the degradation reactions and the scavenger test for determining the dominant reactive oxygen species (ROS) were also demonstrated. The reusability test of the catalyst was performed, and structural stability was confirmed from XRD analysis.

2 Experimental

2.1 Material and methods

The metal oxide was prepared by solution combustion technique which is considered a quick and efficient technique to yield nanoparticles with high phase purity[37]. A detailed procedure of preparing doped and pristine metal oxide by solution combustion technique can be found elsewhere [29]. Ammonium niobate oxalate hydrate (Sigma Aldrich, USA) was used as the precursor for niobium and urea as the fuel. All other chemicals used were of analytical grade. To prepare Nb_2O_5, initially, niobium precursor and urea were dissolved in DI water separately via sonication for 10 min and later mixed together. The mixed clear solution was kept in a preheated muffle furnace at 450°C for 30 min. Black Nb_2O_5 was obtained [38]. This catalyst was then calcined at 550°C for 4 h to obtain white powdered pseudo hexagonal Nb_2O_5 [38]. Metal nitrates were used as the precursors for dopants Sr, Y, Zr and Ag. The atomic doping percentages for metal doped niobia were varied in the range 0.05 - 2.5 % termed as $Nb_{(2-x)}M_xO_{5-\delta}$ where x is the dopant % and M is the dopant. For preparing doped metal oxide the same procedure was used, in addition, the respective dopant's metal nitrate precursor was mixed to the sonicated niobium precursor urea solution.

View Article Online
DOI: 10.1039/C9NA00305C

2.2 Photochemical experiments

To check the photocatalytic activity of pristine and doped Nb_2O_5, a cationic dye MB and an anionic dye OG were taken as model pollutants. The photoreactor set up consisted of a metal halide lamp with an intensity of 121 W/m^2. The actinometry test was performed to check the lamp intensity and the methodology can be found elsewhere [39]. To avoid heating and maintain the reaction at 25°C, the lamp was enclosed in a quartz jacket with inlet and outlet pipes connected to a chiller operating at 10°C. The photodegradation experiments were performed in a quartz beaker. To attain an adsorption-desorption equilibrium, a 2 h dark reaction was performed before photocatalysis. Samples were collected at regular intervals, centrifuged and filtered for subsequent analysis. The degradation of the dyes was analyzed using UV-visible spectroscopy and the degradation of 2-CP was analyzed using HPLC (Waters Inc., USA). The system was equipped with C-18 column with a UV detector and the mobile phase consisted of acetonitrile: water (20:80 v/v) with 0.01 M H_3PO_4 with a flow rate of 0.8 mL min^{-1}.

2.3 Photocatalytic inactivation of bacteria

E. coli strain K-12 MG1655 and *S. aureus* strain ATCC 259323 were taken as model organisms to check the antibacterial response of the photocatalysts. Glasswares, micro tips and other plastics used in the experiment were autoclaved at 120 °C for 2 h. The bacterial cells were incubated in Luria broth under constant agitation at 37 °C for 18 h. Later, the centrifuged washed clean bacterial pellet was suspended in 30 mL of sterile water with a final concentration of ~10^8 CFU/mL. The experiments were conducted under dark for 1 h followed by 1 h of light irradiation under metal halide lamp with an intensity of 15 W/m^2. For analysis, 500 µL of the sample was collected at regular intervals of 20 min and the cell counting was done by the plate count method. The samples were serially diluted with sterile water and 50

μL of diluted samples were plated on solid nutrient agar plates. These plates were incubated at 37 °C for 18 h. Subsequently, the number of viable cells were counted.

3 Characterizations

XRD patterns were obtained using Rigaku diffractometer using Cu-Kα as a source of irradiation. XPS of the materials were recorded using Kratos Axis Ultra DLD instrument with monochromatic Al-Kα X-ray as the energy source (1486 eV). UPS data were obtained using the same instrument with Helium-I source. UV-Vis DRS data were obtained using Shimadzu spectrophotometer (UV 2450). PL spectra of the catalysts were recorded using a Perkin Elmer spectrophotometer. SEM, Carl Zeiss–Ultra 55 FESEM and TEM, Philips CM 200 were used to understand surface morphology of the catalyst. BET surface area assessment was performed using Smart Sorb 92/93 surface area analyzer. TRF data were obtained from Edinburgh Instruments, FLS 920 Spectro fluorimeter using a laser diode for excitation.

4 Results and Discussion

4.1 XRD analysis

To understand the phase purity of the prepared materials, XRD analysis was done. In Fig.1, the XRD diffraction patterns of pristine and doped Nb_2O_5 nanoparticles with 0.25 atom % metal ions (Sr, Y, Zr, Ag) were compared. All the diffractions patterns correspond to pure crystalline hexagonal Nb_2O_5 phase (JCPDS no 28-0317) and no possible impurity phase was found in the samples. The predominant peak of Nb_2O_5 at $2\theta = 28.52^o$ corresponding to (1 0 0) plane can be seen to shift to lower diffraction angles 28.27^o, 28.35^o, 28.43^o and 28.34^o when doped with Sr^{2+}, Y^{3+}, Zr^{4+}, and Ag^{+} respectively. This can be attributed to the lattice strain generated due to larger ionic radii of the dopants as compared to Nb^{+5} [40]. The ionic radii of Nb^{5+}, Sr^{2+}, Y^{3+}, Zr^{4+}, and Ag^{+} are 69 pm, 112 pm, 90 pm, 72 pm, and 126 pm respectively [41]. The increase in the lattice parameters obtained from Rietveld refinement of the XRD patterns

View Article Online
DOI: 10.1039/C9NA00305C

can be found in Table 1. These dopants substitute Nb^{5+} ions in their lattice sites causing a change in d-spacing and subsequently shifting XRD peaks to lower angles [42].

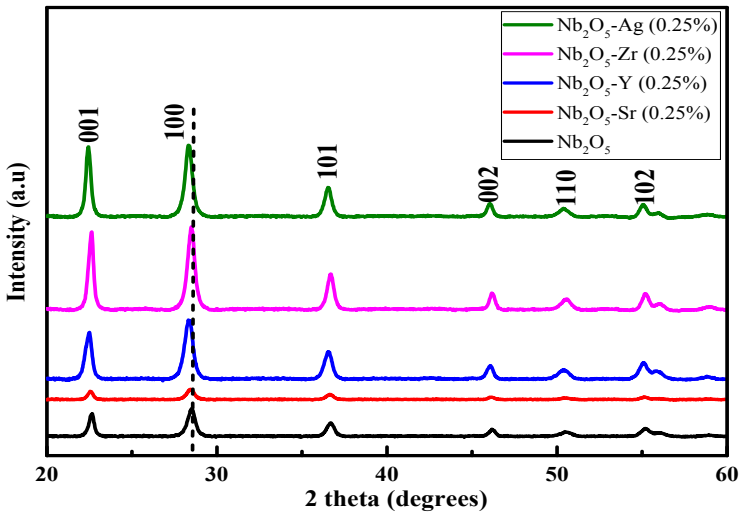

Fig. 1 XRD patterns of Nb_2O_5 doped with Sr, Y, Zr, and Ag of 0.25 atom %

4.2 XPS analysis

XPS was performed to obtain the oxidation state of the elements present in the material. In Fig. 2 (a) the peaks at binding energy 207.02 eV and 209.8 eV correspond to Nb-$3d_{5/2}$ and Nb-$3d_{3/2}$ with spin-orbit splitting of 2.78 eV [43]. This confirms the element to be present in the +5 oxidation state. In Fig. 2 (b) the peak at binding energy 529.9 eV can be assigned to lattice oxygen. The O-1s peak at 531.5 eV can be related to surface hydroxyl groups [44]. The XPS signals of the dopants were not detected due to low atomic concentration.

4.3 UV-Vis DRS

UV-Vis DRS analysis can be utilized to compare the shift in the absorption spectra for pristine and doped Nb_2O_5. Fig S1 (a) shows the absorption spectra of Sr-doped Nb_2O_5. It can be seen that with the increase in dopant concentration, the absorption edge of Nb_2O_5 was slightly red shifted but as the dopant concentration was increased to 2.5 %, the absorption edge tends to shift to the lower wavelength signifying an increase in the band gap. This could

View Article Online
DOI: 10.1039/C9NA00305C

be due to the formation of a minute amount of strontium oxide. A similar trend was observed for Y and Zr doped Nb_2O_5 as shown in Fig. S1 (b) and (c). From literature strontium oxide, yttrium oxide and zirconium oxide are semiconductors with a band gap of 5.5 eV [45], 5.17 eV [46] and 5 eV [47] respectively which are relatively higher than that of niobium oxide. Therefore if the concentration of these dopants is increased beyond a certain limit, a minute formation of these oxides might occur on the surface of Nb_2O_5 causing a shift in the absorption edge of Nb_2O_5 to lower wavelength region. However, silver oxide possesses a band gap smaller than Nb_2O_5 of around 2.25 eV [48], therefore from Fig. S1 (d), with the increase in Ag^+ concentration in Nb_2O_5, absorption edge was found to continue to shift to a higher wavelength even at higher dopant concentration. From this analysis, it can be assumed that 0.25 atom % could be the optimized dopant concentration for Sr^{2+}, Y^{3+}, and Zr^{4+} in Nb_2O_5, but for Ag^+ the optimized dopant concentration can be concluded from further analyses. However, experimentally from MB degradation reactions in photocatalysis section, Ag^+ at 0.1 atom % in Nb_2O_5 was found as the optimized dopant concentration.

To compare the band gap of the different dopants in Nb_2O_5 with the optimized concentration, their absorbance spectra were shown in Fig. 3. The curve for doped Nb_2O_5 was red-shifted relative to pristine Nb_2O_5 from 417 nm to 420 nm, 422 nm, 423 nm and 427 nm due to the incorporation of Ag (0.1%), Y (0.25 %), Sr (0.25 %) and Zr (0.25%) dopants respectively. This red shift suggests a slight reduction in the band gap of Nb_2O_5. The optical band gap was obtained using the Tauc plot [49] $(F(R) * h\nu)^{1/n}$ vs. hν as shown in the inset of Fig. 3. Here hν is photon energy in eV and F(R) is Kubelka Munk function shown in Eq. (1) which determines the extent of photon absorption of a semiconductor from its reflectance. From DFT studies, Nb_2O_5 was found to possess an indirect band gap [50], therefore, n is taken to be 2 for indirect transitions [49]. From the Tauc plot, the band gap (E_g) of the combustion synthesized Nb_2O_5 was found to be 3 eV and for doped Nb_2O_5, a slight shift in the band gap

View Article Online
DOI: 10.1039/C9NA00305C

was observed as shown in table 1. The reduction in the band gap could be attributed to the insertion of Sr, Y, Zr or Ag cations into the Nb_2O_5 lattice. Since the conduction band minimum is made up of Nb 4d bands [51], the substitution of Nb^{5+} with these cations might induce their energy states to extend into the Nb_2O_5 conduction band, resulting in the narrowing of the band gap. The maximum reduction in the band gap was observed for Zr (0.25%) followed by Sr (0.25%), Y (0.25%) and Ag (0.1%). Decreasing the band gap helps the materials to absorb light in the visible region but this could also lead to faster recombination of charge carriers. Therefore other parameters which are crucial for the photoactivity of a semiconductor such as BET surface area and lifetime of charge carriers are discussed in a later section.

$$F(R) = (1-R)^2/2R \quad (1)$$

4.4 UPS analysis

UPS technique can be employed to understand the valence band properties of a semiconductor. Fig. 4 represents the UPS spectrum of Nb_2O_5 where the peak at binding energy 14.8 eV was due to hybridization between O-2p and Nb-4d bond. The peak at 12 eV is formed by the O-2p orbital. The peak at around 8 eV is from the O-2p in the valence band region. These analyses could be found elsewhere which were obtained comparing UPS spectrum with DOS results [52]. UPS analysis can also be utilized to obtain the exact band edges of a semiconductor [53]. The work function(W_f) of a semiconductor surface is given by Eq. (2) where hν is the energy of photons from Helium I source and SECO is secondary electron cut off energy which is obtained from a linear extrapolation of the higher emission onset edge to zero intensity of higher binding energy[54]. Here hν is 21.22 eV and SECO is 18.44 eV, thus W_f is 2.78 eV. The lower emission onset energy (E_2) is obtained by linear extrapolation of the intensity curve tangent to the baseline[49] and it is obtained at 4.2 eV. From DRS, the band gap of Nb_2O_5 is found to be 3 eV, thus from Eq. (3) and Eq. (4) the energy

View Article Online
DOI: 10.1039/C9NA00305C

level of valence band maximum (E_{vb}) is obtained at -6.98 V and conduction band minimum (E_{cb}) at -3.98 V vs Absolute vacuum scale (AVS).

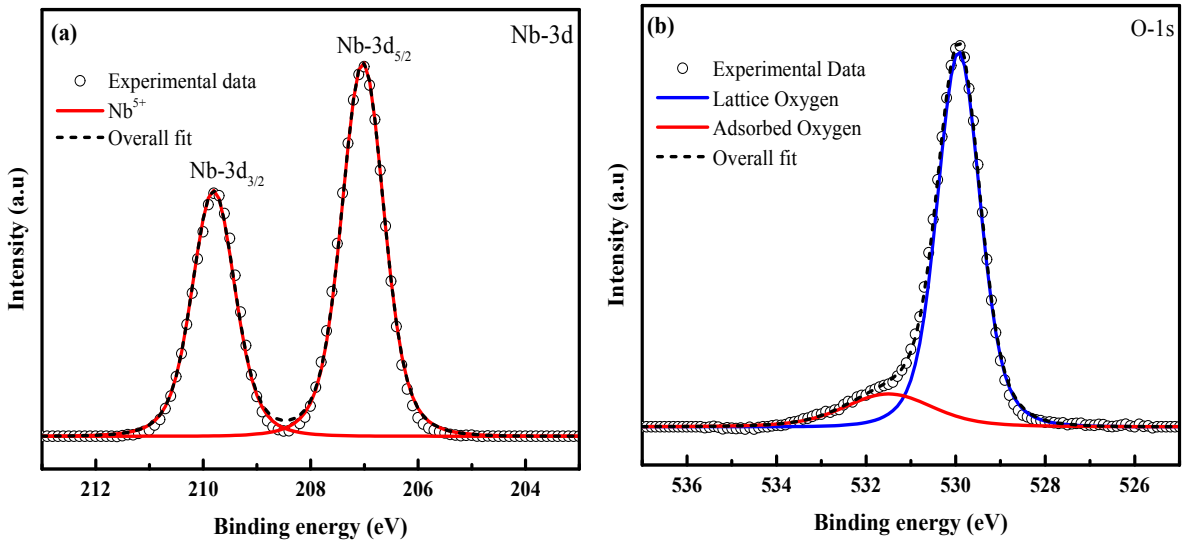

Fig. 2 XPS spectra of (a) Nb-3d and (b) O-1s

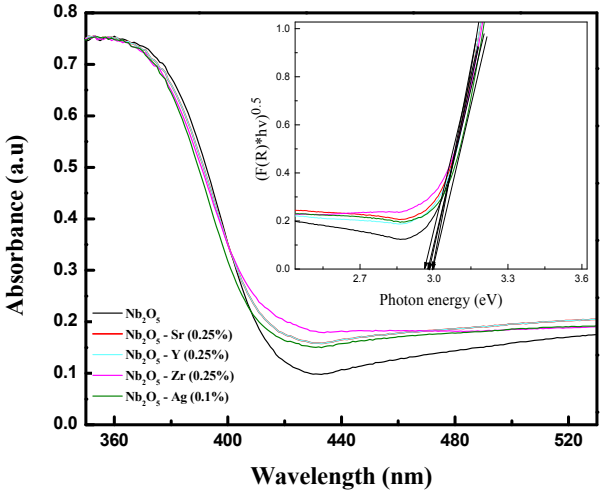

Fig. 3 UV-Vis absorbance spectra of pristine and doped Nb_2O_5 and inset represents transformed Kubelka munk function vs. photon energy

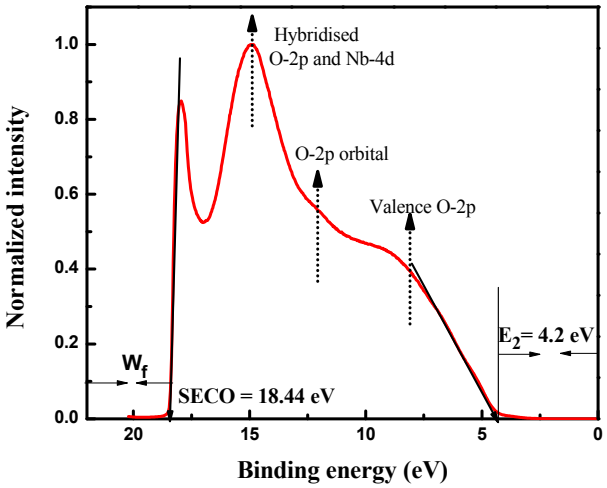

Fig. 4 UPS spectra of Nb_2O_5

$$W_f = 21.22 - SECO \quad (2)$$

$$E_{vb} = W_f + E_2 \quad (3)$$

$$E_{cb} = V_b - E_g \quad (4)$$

View Article Online
DOI: 10.1039/C9NA00305C

4.5 BET surface area

From BET surface area measurements shown in Table 2, it could be concluded that the surface area of Nb_2O_5 was enhanced when doped with Sr^{2+}, $Y^{3+,}$ and Zr^{4+} metal ions. No significant variation in the surface area was observed from the increase in the dopant concentration. However, for Ag^{+} doped Nb_2O_5, with the increase in the dopant concentration from 0.1 % to 0.25 %, the surface area was increased to 1.4 times but and then decreased by 1.7 times when the concentration was increased to 2.5%. This could be due to agglomeration resulting in a decrease in the surface area[55]. On comparing the surface area of the dopants with optimised dopant concentration in Nb_2O_5, the following trend can be concluded Sr (0.25%) > Zr (0.25%) > Y (0.25%) > Ag (0.1%). Along with the increase in the surface area, analysis of the lifetime of charge carriers is important for determining the photoactivity of the material as these parameters need not be directly proportional to each other. To determine the presence of defects and recombination time of exciton, PL and TRF analyses are discussed in the later section.

4.6 PL analysis

From photoluminescence analysis, information on the photochemical properties of a semiconductor such as oxygen vacancies, defects, charge carrier transfer can be obtained [56]. Nb_2O_5 with excitation wavelength 325 nm was found to exhibit photoluminescence in the range from 350 to 550 nm as shown in Fig. 5. The short wavelength emissions at 409 nm can be attributed to the near band edge emissions where electron transitions take place from bottom of conduction band to the top of valence band [56]. The emission spectra at 448, 466, 480, 490 and 560 nm can be related to surface defects and oxygen vacancies [56, 57] where

View Article Online
DOI: 10.1039/C9NA00305C

transitions occur in the energy levels within the band gap [58]. No new PL signal was observed from the doped metals but variation in intensity was found. The intensities of Zr (0.25%) and Y (0.25%) doped Nb_2O_5 were found to be higher than Nb_2O_5. This could be due to the higher content of surface defects and oxygen vacancies that are the source of non-radiative recombination [58] and possibly not due to higher recombination rate as evident from recombination time of charge carriers from TRF analysis. The intensities of Sr (0.25%) and Ag (0.1%) doped Nb_2O_5 were found to be lower signifying lower recombination rate of excitons than Nb_2O_5.

4.7 Charge carrier dynamics by TRF analysis

The lifetime of charge carriers can be obtained from TRF analysis. The lifetime emission decays of pristine and metal-doped Nb_2O_5 spectra were measured at maximum emission wavelength 415 nm (as obtained from PL analysis) using 305 nm laser diode. Fig. 6 shows the TRF decay curve for Nb_2O_5. The decay curve was fitted using two parameters biexponential decay model Eq. (5) with R^2 higher than 0.97. Here A_1 and A_2 are the decay constants, the shorter lifetime τ_1 corresponds to the non-radiative process which is due to heat losses and longer lifetime τ_2 corresponds to the radiative process which provides information

$$y = A_1 \exp(-t/\tau_1) + A_2 \exp(-t/\tau_2) \quad (5)$$

$$\tau_{avg} = (A_1 * \tau_1^2 + A_2 * \tau_2^2) / (A_1 * \tau_1 + A_2 * \tau_2) \quad (6)$$

related to the electron-hole recombination [59]. The average lifetime was calculated using Eq. (6) [60]. The lifetime of charge carriers (τ_{avg}) is shown in Table 2. For Nb_2O_5, τ_{avg} was found to be 1088 picoseconds (ps) and with the incorporation of dopants in the host Nb_2O_5, the lifetime of charge carriers were found to have increased. Indeed Sr (0.25%), Y (0.25%), Zr (0.25%) and Ag (0.1 %) were found to have longer lifetime compared to 0.1% and 2.5% dopant concentration. With the excess dopant concentration of 2.5%, τ_{avg} decreased as the

View Article Online
DOI: 10.1039/C9NA00305C

increased dopant concentration must have acted as the recombination centers. On comparing the lifetimes of optimised dopants the following trend can be observed Sr (0.25%) > Y (0.25%) > Zr (0.25%) > Ag (0.1%). The significance of the longer lifetime of charge carriers vs. photoactivity of the catalysts towards different pollutants is discussed in the photocatalysis section.

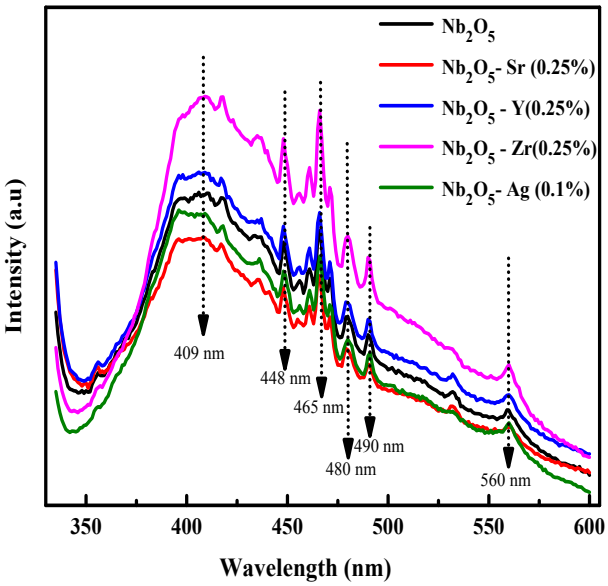

Fig. 5 PL spectra doped and pristine Nb_2O_5

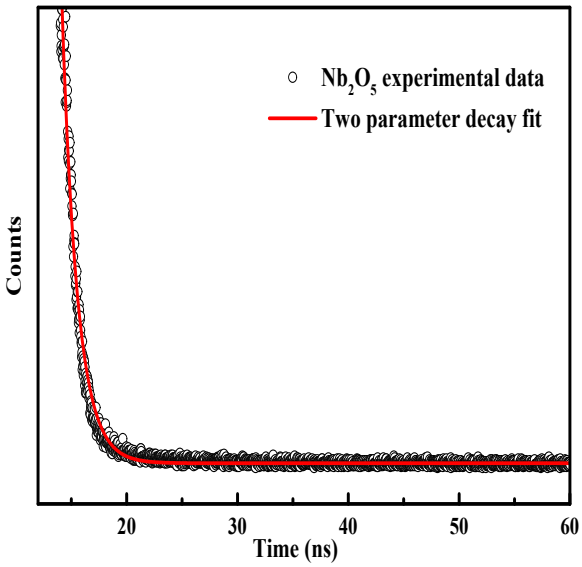

Fig. 6 TRF decay curve of Nb_2O_5

4.8 SEM and TEM analysis

Fig. 7 (a) and (b) shows the SEM images of Nb_2O_5 and Sr (0.25%) doped Nb_2O_5 nanoparticles which are found to have earth rock like structure. No specific morphology change was observed due to the incorporation of dopants. The SEM images for the other doped materials are shown in Fig S2 (a), (b) and (c). The d spacing of 3.0 Å and 3.9 Å obtained from HR TEM images in Fig. 7 (c), (d) correspond to planes (1 0 0) and (0 0 1) respectively, and the inset shows the FFT images. These planes with the respective d spacing can be validated from the XRD patterns.

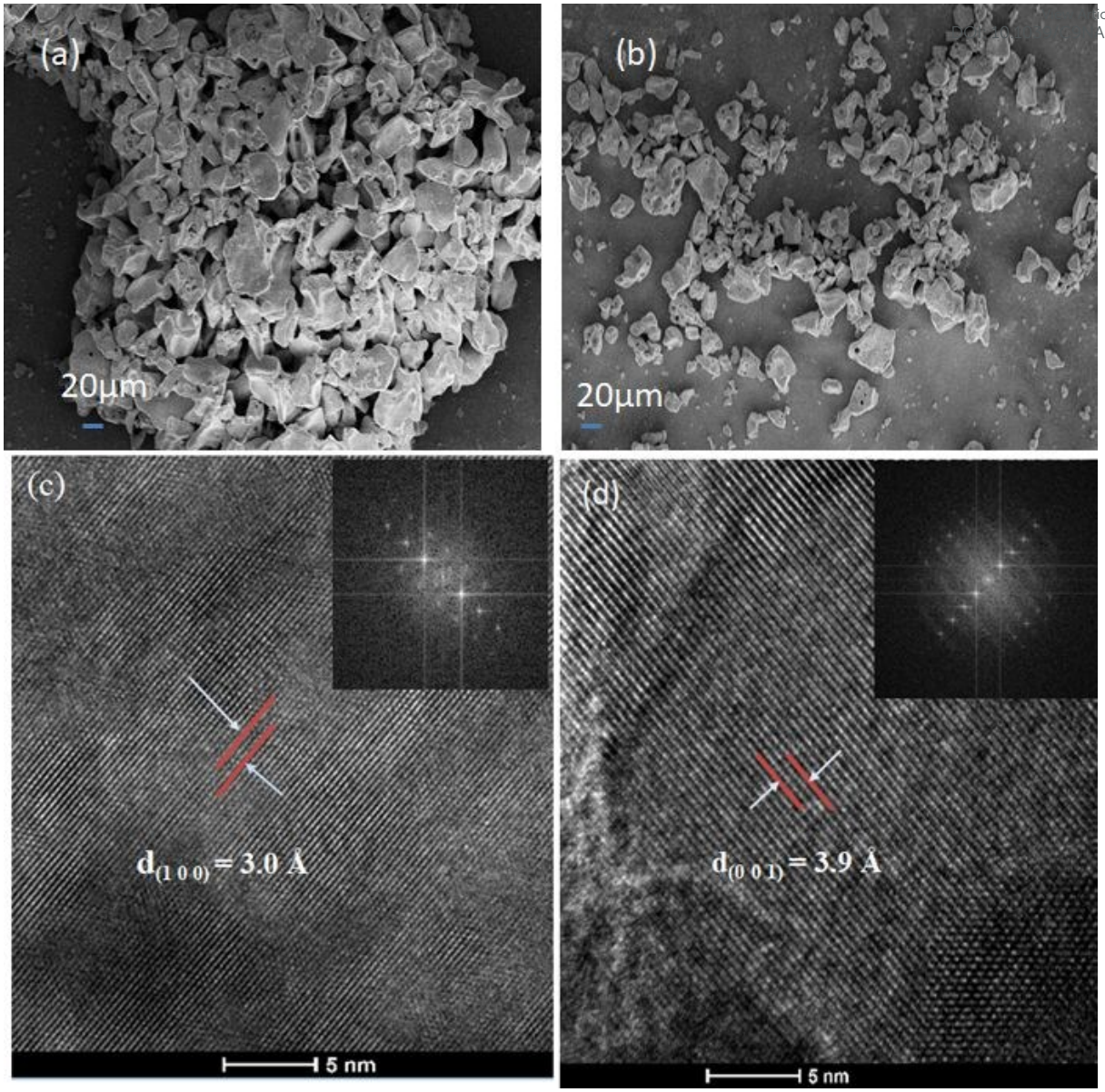

Fig. 7 (a) SEM image of Nb_2O_5, (b) SEM image of Sr (0.25%)-Nb_2O_5, (c) HRTEM image of Nb_2O_5 showing d spacing of (1 0 0) plane and inset is the FFT image, (d) HRTEM image of Nb_2O_5 showing d spacing of (0 0 1) plane and inset represents the FFT image

4.9 Photocatalysis

4.9.1 MB photo degradation

4.9.1.1 Effect of catalyst loading

The degradation of MB was evaluated by monitoring the decrease in absorbance peak at 665 nm using UV-visible spectroscopy. Fig. S3 in the electronic supporting information

View Article Online
DOI: 10.1039/C9NA00305C

(ESI) represents the effect of catalyst loading for the degradation of MB with an initial concentration of 15 ppm. The experiment was carried out at a neutral pH of 7. The zero-point charge (pH_{zpc}) of Nb_2O_5 (as obtained from the pH drift method [62]) is 4 shown in Fig. S4. The surface of Nb_2O_5 is positively charged at pH below pH_{zpc} and negative above pH_{zpc} [53]. Therefore, MB which is a cationic dye gets adsorbed readily on the surface of Nb_2O_5 at pH 7. For control, photolysis was performed which showed no degradation of the dye. Adsorption-desorption equilibrium for the catalyst was achieved in 2 h of reaction under dark conditions. Catalyst loading of 0.2 g/L degraded the dye by 20 % at the end of 2 h. This lower catalyst loading was not sufficient to generate enough ROS to degrade the dye. A loading of 0.5 g/L degraded the dye by 46 %. On further increasing the catalyst loading to 1 g/L, the solution became turbid. This hindered penetration of light which resulted in a decrease in activity, thereby degrading the dye by 44 % at the end of 2 h [63]. Therefore, 0.5 g/L was taken as the optimum catalyst loading to perform further experiments.

4.9.1.2 Optimization of Sr, Y, Zr and Ag concentration doped in Nb_2O_5 towards MB degradation

To inhibit charge carrier recombination, optimization of dopant concentration is necessary for achieving higher photocatalytic activity [30]. Fig.S5 (a) shows the effect of Sr doping concentration in Nb_2O_5 for MB photodegradation. Sr content at 0.25% was found to be the optimized concentration and the same was observed for Y and Zr doped Nb_2O_5 from Fig. S5 (b) and S5 (c). This could be attributed to the greater number of active sites at this dopant concentration as evident from the 2 h of dark adsorption. As the dopant concentration was increased to 2.5 %, the photocatalytic activity for all the above dopants decreased which is also complemented by TRF analysis. The reduction in the distance between the trap sites resulted in faster electron-hole recombination as the excess dopant concentration acted as the recombination centers [61]. For Ag-doped Nb_2O_5 the optimized dopant loading was 0.1%

View Article Online
DOI: 10.1039/C9NA00305C

shown in Fig. S5 (d). When the loading increased beyond the optimal level, reduction in the activity could be due to faster recombination. Therefore, when Ag loading is increased, clusters of Ag species form overlapping agglomerates which shadow the photocatalytic activity due to surface plasmon absorption [64].

4.9.1.3 Rate kinetics for MB adsorption and photodegradation using optimized dopant concentration

The adsorption of MB on metal doped Nb_2O_5 shown in Fig. S6 was found to follow Lagergren's pseudo-first-order reaction model Eq. (7), where k_a is adsorption rate constant (min^{-1}), q_e and q_t are the amounts of adsorbed dye (mg/g) at equilibrium and at time t [65]. Following adsorption, the photodegradation of MB shown in Fig. 8 followed Langmuir Hinshelwood model Eq. (8) [66]. Here k_m is the photodegradation rate constant and

$$\ln (q_e - q_t) = \ln (q_e) - k_a t \quad (7)$$

$$\ln (C_0/C) = k_m t + \ln (C_0/C_1) \quad (8)$$

C_0 is the initial dye concentration. C_1 and C are the concentration at reaction time zero and at time t. The rate constants for MB adsorption and photodegradation kinetics are shown in Table 2. The rate constants for photodegradation of the dye were found to follow the order Sr > Ag >Zr > Y. However, from TRF analysis, the lifetime of the charge carriers followed the order Sr > Y > Ag > Zr. The non-complementary relation between the photoactivity and the lifetime of charge carriers could be the presence of deep trap states in the catalyst. The electrons trapped in these states show longer lifetime but are unable to reduce electron acceptors, thus lowering the efficiency of photocatalytic reactions [67]. The number of active sites for adsorption, increase in surface area and the lifetime of charge carriers all play roles

View Article Online
DOI: 10.1039/C9NA00305C

in degrading the pollutant. It would be difficult to identify the dominant property of the material for the activity towards pollutant degradation.

4.9.2 OG photodegradation: Effect of pH and dopants

The initial concentration of OG was taken as 20 ppm. The photodegradation of the dye was monitored by checking the absorbance at 480 nm using UV-Vis spectroscopy. OG is an anionic dye and at neutral pH of 7.6, with an optimized catalyst loading of 1.2 g/L (Fig S7), the dye was degraded only by 2 % as seen from Fig. S8. With the decrease in pH, the degradation increased. Maximum degradation of 30% was observed at pH 3.25. However, at very low pH of 2.5, the catalyst surface was masked by a greater number of H^+ adsorbing on it preventing the photoexcitation of Nb_2O_5 leading to decrease in the photocatalytic activity. Similar phenomena were observed in some other studies [68].

Fig. 9 represents the photodegradation profile of OG with Nb_2O_5 doped with Sr, Y, Zr, and Ag with the optimized concentration of the dopants at pH 3.25 and a loading of 1.21 g/L. No significant discoloration of the dye was observed in the 2 h of dark reaction. For control, photolysis was performed which showed no degradation of the dye. The doped material was found to perform better than pristine Nb_2O_5 following the order Sr > Zr~Y > Ag > pristine Nb_2O_5. This order could be attributed to the same increasing trend in the surface area of the doped catalyst. The photodegradation of OG was found to follow 1st order kinetics Eq. (9), where k_o is the rate constant, C_o is the initial concentration and C is the concentration at time t. The rate constants are shown in Table 3.

$$\ln (C/C_0) = - k_o t \quad (9)$$

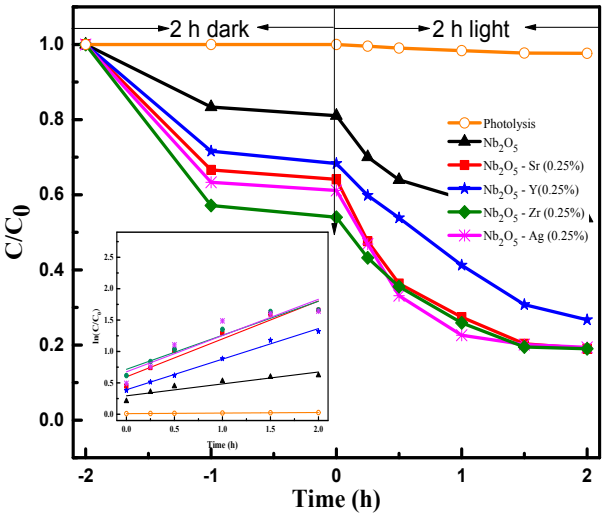

Fig. 8 Effect of dopants in Nb_2O_5 for MB degradation and inset represents rate kinetics

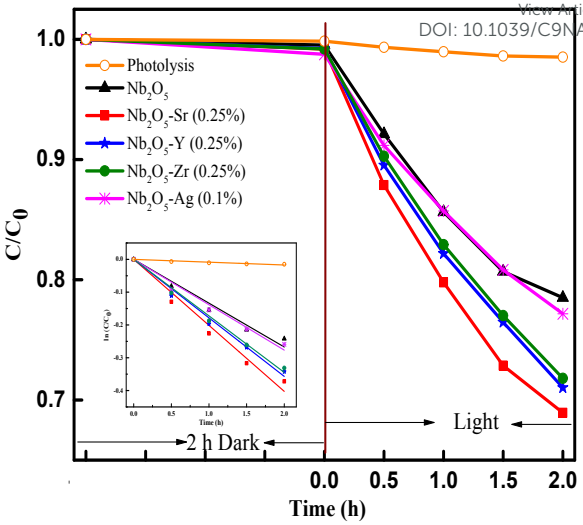

Fig. 9 Effect of dopants in Nb_2O_5 for OG degradation and inset represents rate kinetics

4.9.3 IC photodegradation

The initial concentration of IC was taken as 40 ppm. The photodegradation of the dye was monitored by checking the absorbance at 610 nm using UV-Vis spectroscopy. Since IC is also an anionic dye, no degradation of the dye was observed at neutral pH of 7.5. From Fig. S9, around maximum degradation of the dye, was observed at pH 3 with a catalyst loading of 0.5 g/L. The doped materials were found to perform better than pristine Nb_2O_5, Fig. 10 following the order Sr > Zr > Y > Ag > pristine Nb_2O_5 following 1st order kinetics Eq. (10) with a maximum degradation of 95% from Sr (0.25%) doped Nb_2O_5) where k_i is the rate constant for IC photodegradation. The rate constants are shown in Table 3.

$$\ln (C/C_0) = - k_i t \qquad (10)$$

4.9.4 2-CP photodegradation

The photodegradation of 2-CP was analyzed using HPLC with an initial concentration of 25 ppm. Adsorption-desorption equilibrium was observed in 2 h of dark reaction. Fig. 11 represents the effect of pristine and doped Nb_2O_5 for 2-CP photodegradation and inset

View Article Online
DOI: 10.1039/C9NA00305C

represents the rate kinetics. Around 90% degradation of the pollutant was observed from the doped catalysts as compared to 15% degradation from photolysis and around 50 % from pristine Nb_2O_5. The photodegradation followed 1st order kinetics Eq. (12), where k_p is the rate constant at neutral pH of 7.3 and catalyst loading of 0.5 g /L. The rate constants are shown in Table 3 following the order Sr > Zr >Y > Ag > Nb_2O_5

$$\ln (C/C_0) = - k_p t \quad (12)$$

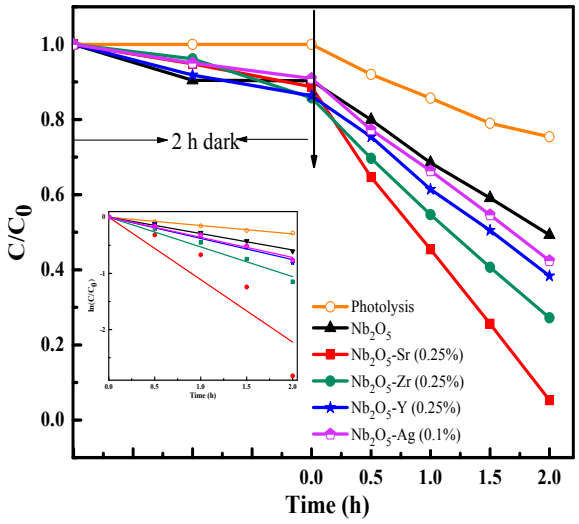

Fig. 10 Effect of dopants in Nb_2O_5 for IC degradation and inset represents rate kinetics

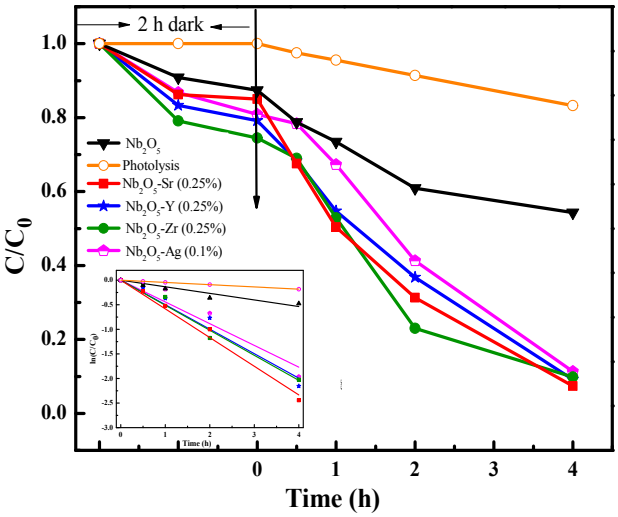

Fig. 11 Effect of dopants in Nb_2O_5 for 2-CP degradation and inset represents rate kinetics

4.9.5 Antibacterial experiments

To assess the antibacterial response of the catalysts, *E. Coli* was taken as a model gram-negative bacteria. Fig. S10 represents the effect of catalyst loading Sr (0.25%) doped Nb_2O_5 for the photoinactivation of *E. coli*. Initial bacterial concentration was taken as $2x10^8$ CFU/mL. It was observed that the loading of 0.05 g/L was too low to inactivate bacteria and 0.25 g/L caused turbidity causing a decrease in the rate of inactivation. The optimized loading was found to be 0.1 g/L resulting in a 3.5 log reduction of *E. coli* cells. Fig. 11 shows the effect of different dopants in Nb_2O_5 for *E.coli* photoinactivation and inset represents the rate

View Article Online
DOI: 10.1039/C9NA00305C

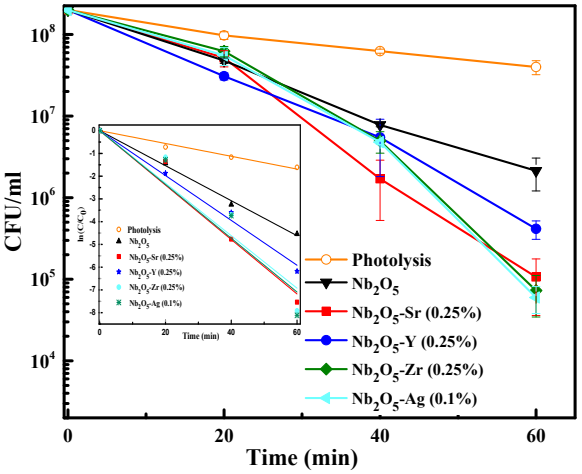

Fig. 11 Effect of dopants in Nb_2O_5 for *E. coli* inactivation and inset represents rate kinetics

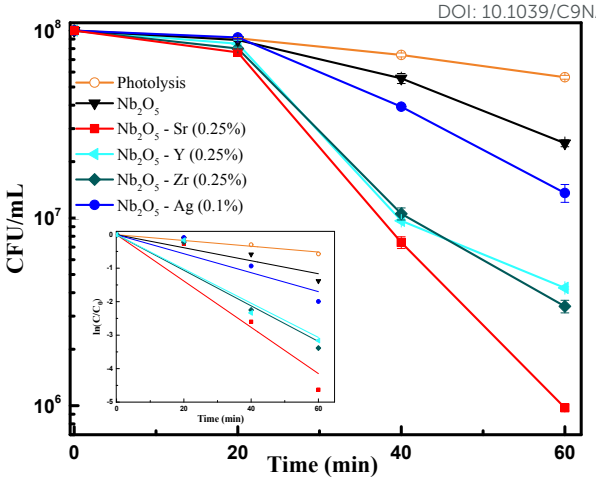

Fig. 12 Effect of dopants in Nb_2O_5 for *S.aureus* inactivation and inset represents rate kinetics

kinetics. For control, photolysis was performed and less than 1-log reduction was observed. A 1.5-log reduction in bacterial cells was observed with Nb_2O_5. The doped material was found to perform better than Nb_2O_5 with rate constants following the order Sr ~Zr~ Ag > Y > Nb_2O_5. Around 3.5 log reduction was observed from Ag, Zr and Sr-doped Nb_2O_5 and a 3-log reduction were found from Y doped Nb_2O_5. However, when a model gram-positive strain *S. aureus* was taken with an initial count of 10^8 CFU/mL, the bactericidal efficacy was maximum of ~2 log folds from Sr doped Nb_2O_5 as shown in Fig.12. From photolysis, insignificant reduction in *S.aureus* cells was observed and around 0.5 log reduction from pristine Nb_2O_5. Since the major bacterial contamination pertaining in the domestic water system is by fecal coliforms and not predominantly due to gram-positive species[4, 69], our catalyst can remediate water effectively. The photoinactivation of *E. coli* and *S. Aureus* were found to follow 1st order kinetics fitting the data using Eq. (11) and Eq. (12) where k_e and k_s are the rate constants for *E.coli* and *S.aureus* respectively, C_o is the initial concentration and C is the concentration at time t. The rate constants are shown in Table 3.

$$\ln (C/C_0) = - k_e t \qquad (11)$$

$$\ln (C/C_0) = - k_s t \quad (12)$$

View Article Online
DOI: 10.1039/C9NA00305C

4.10 Scavenger test

To identify the active species taking part in the photodegradation reactions, trapping experiments were carried out. MB *and E.coli* were taken as the test pollutants and Sr (0.25%) doped Nb_2O_5 as the catalyst. 1 mM t-butanol [70], 1 mM EDTA-Na [70] and 2 mM TEMPO [71] were used as scavengers for ·OH, h^+ and $O_2^{\cdot-}$ radicals respectively in the photoreaction containing the dye/*E.coli* and the catalyst in the presence of light. Control experiments

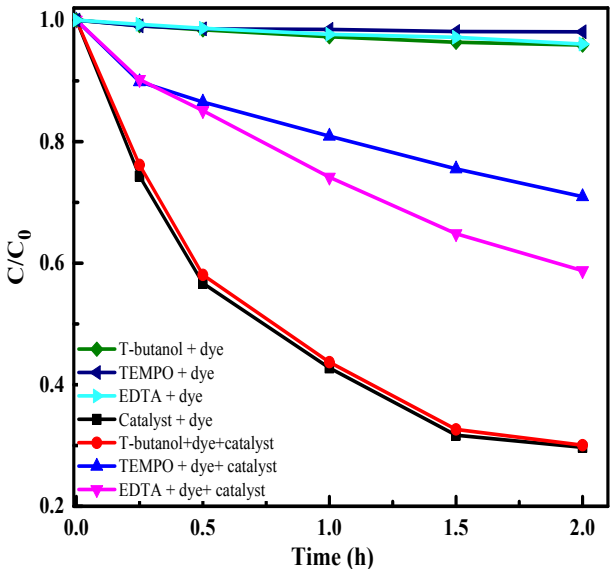

Fig. 13 Radical trapping experiment with scavengers and MB as the pollutant

included reaction in the presence of scavenger, dye/*E.coli* and light without the catalyst and it was observed that there was insignificant dye degradation or bacteria inactivation from Fig. 13 and Fig. S11. The main active species identified was superoxide radical suppressing the degradation rate of the dye by ~60 %. Generation of superoxide radicals at -4.17 V vs AVS scale was evident from UPS analysis. The holes were also capable to directly oxidize the pollutant as the scavenger EDTA could prevent the dye degradation by 40%. In case of antibacterial experiments as well, superoxide radicals and holes were found to be the main

View Article Online
DOI: 10.1039/C9NA00305C

active species. Scavengers TEMPO and EDTA were found to suppress the inactivation by almost 90%.

4.11 Proposed Mechanism

A possible mechanism is proposed using the combined analysis from PL, DRS, UPS, TRF and scavenger tests. A schematic of such a mechanism with energy levels of Nb_2O_5 is shown in Fig. 14. The as prepared Nb_2O_5 nanoparticles were found to absorb in the near visible region with a band gap E_g of 3 eV and energy levels of conduction band minimum E_{cb} at -3.98 V and that of valence band maximum E_{vb} at -6.98 V vs AVS. The conduction band of Nb_2O_5 is made up of Nb-4d orbitals and valence band consists of O-2p orbitals [51]. When photons (hν) with energy equal or greater than 3 eV is incident on Nb_2O_5, electronic transitions can take place from E_{vb} to E_{cb} of the semiconductor or to the defect states. The presence of defects in Nb_2O_5 semiconductor was detected from PL analysis generated due to the presence of vacancies, impurities or interstitial atoms [72]. These defects lying near E_{cb} or E_{vb} can capture the electrons or the holes evading charge recombination. Also, incorporation of dopants induces its own energy states in the semiconductor which captures the photoinduced electrons. This enhances charge separation resulting in prolonged recombination time validated from TRF analysis. The orbitals of the dopants Sr, Y, Zr, and Ag could be lying around or merging with Nb-4d orbitals of Nb_2O_5 as a slight reduction in the band gap of Nb_2O_5 was observed on doping. These trapped electrons or the electrons in E_{cb} can react with oxygen to produce $O_2^{\cdot-}$ radicals which are the main active species responsible for organic pollutants photodegradation as well as for bacteria inactivation. The other active species as evident from scavenger experiments are the positive holes which are created in the E_{vb} or the trapped holes that could directly attack the pollutants [73].

View Article Online
DOI: 10.1039/C9NA00305C

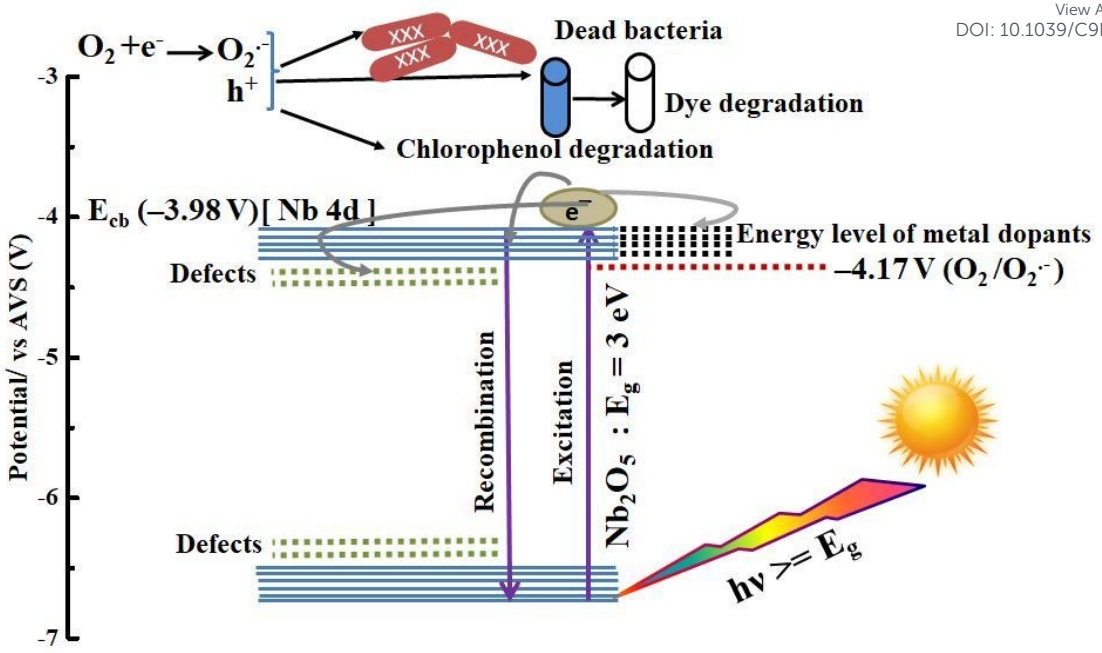

Fig. 14 Photocatalysis mechanism in metal-doped Nb_2O_5

4.12 Reusability and structural stability

Fig. S12 shows the reusability of Sr 0.25% doped Nb_2O_5 catalyst for the degradation of MB. After five cycles the catalyst could degrade the dye by 70 %, the activity was found to decrease only by 12.5 % compared to the fresh catalyst. Fig. S13 shows the XRD pattern of the catalyst before and after use for 5 cycles. No change in the pattern was observed confirming its stability.

View Article Online
DOI: 10.1039/C9NA00305C

Table 1: Lattice parameters and particle size for pristine and doped Nb_2O_5

Catalyst	a(Å)	b(Å)	c(Å)	Band gap (eV)
Nb_2O_5	3.6115	3.6115	3.9269	3.00
Nb_2O_5-Sr (0.25%)	3.6121	3.6121	3.9282	2.95
Nb_2O_5-Y (0.25%)	3.6132	3.6131	3.9295	2.96
Nb_2O_5-Zr (0.25%)	3.6216	3.6216	3.9396	2.94
Nb_2O_5-Ag (0.25%)	3.6133	3.6133	3.9306	2.96

Table 2: BET surface area and TRF charge carrier dynamics of doped and pristine Nb_2O_5, rate constant of MB photodegradation

Catalyst	BET surface area (+1 m^2/g)	Lifetime of charge carriers τ_{avg} (ps)	MB adsorption rate constant k_a (+ 0.1 h^{-1})	MB photodegradation rate constant k_m (+ 0.05 h^{-1})
Photolysis	-	-	-	0.01
Nb_2O_5	28	1088	1.6	0.19
Nb_2O_5-Sr (0.1%)	32	1223	-	0.42
Nb_2O_5-Sr (0.25%)	43	1290	2.3	0.60
Nb_2O_5-Sr (2.5%)	44	1212	-	0.41
Nb_2O_5-Y (0.1%)	38	1047	-	0.30
Nb_2O_5-Y (0.25%)	36	1241	2.2	0.49
Nb_2O_5-Y (2.5%)	33	1127	-	0.46
Nb_2O_5-Zr (0.1%)	36	1143	-	0.43
Nb_2O_5-Zr (0.25%)	38	1162	2.4	0.54
Nb_2O_5-Zr (2.5%)	41	904	-	0.42
Nb_2O_5-Ag (0.1%)	32	1202	2.3	0.58
Nb_2O_5-Ag(0.25%)	45	1029	-	0.47
Nb_2O_5-Ag (2.5%)	26	1084	-	0.40

View Article Online
DOI: 10.1039/C9NA00305C

Table 3: Rate constants for OG, IC, 2-CP , *E. coli and S.aureus* inactivation

Catalyst	OG degradation rate constant k_o (+ 0.01 h^{-1})	IC degradation rate constant k_i (+ 0.01 h^{-1})	2-CP degradation rate constant k_c (+ 0.01 h^{-1})	*E.coli* inactivation rate constant k_e (+ 0.01 min^{-1})	*S.aureus* inactivation rate constant k_s (+0.005 min^{-1})
Photolysis	0.008	0.14	0.04	0.027	0.008
Nb_2O_5	0.134	0.29	0.13	0.076	0.019
Nb_2O_5-Sr (0.25%)	0.201	1.11	0.58	0.120	0.069
Nb_2O_5-Y (0.25%)	0.178	0.37	0.49	0.098	0.028
Nb_2O_5-Zr (0.25%)	0.172	0.52	0.50	0.115	0.053
Nb_2O_5-Ag (0.1%)	0.138	0.35	0.44	0.118	0.051

Conclusions

This study presents the optical and photocatalytic properties of solution combustion synthesized Nb_2O_5 nanoparticles. The derived photocatalyst exhibited a band gap of 3 eV with valence band edge at -6.98 V and conduction band edge at -3.98 V vs AVS signifying the energy level to be sufficient enough to generate superoxide radicals at -0.417 V. The work function of the material was found to be 2.78 eV. Several properties of this host material were influenced on doping with metals (Sr, Y, Zr, and Ag) such as increment in the lattice parameters as analyzed from Rietveld refinement of the XRD patterns of pristine and doped Nb_2O_5, enhancement in the surface area from BET analysis. A red shift in the absorption edge of Nb_2O_5 on doping was found from DRS analysis. The as-prepared niobium

View Article Online
DOI: 10.1039/C9NA00305C

oxide was found to have surface defects and oxygen vacancies from PL analysis. Doping Nb_2O_5 with metals facilitated better charge separation and the optimized concentration of dopants Sr^{2+}, Y^{3+} and Zr^{4+} were found to be 0.25 % and 0.1 % for Ag^{+} dopant as analyzed from TRF technique. The optimization of this dopant concentration was also validated experimentally by analyzing MB photodegradation. The doped materials showed excellent photoactivity towards dye and chlorophenol degradation as well as bacteria inactivation. The affinity of these materials towards the degradation of each pollutant was different, but Sr (0.25%) doped Nb_2O_5 was found to be the best amongst all the other catalysts. From scavenger test, superoxide radical and holes were found to be the dominant reactive oxygen species in the photodegradation reactions. The catalyst was found to be stable after 5 cycles and the structural stability was confirmed from XRD analysis. This study suggests that combustion synthesized Sr (0.25%) doped Nb_2O_5 is chemically stable and could be used as a potential photocatalyst for antimicrobial action and degradation of recalcitrant organic contaminants.

Acknowledgments

The authors would like to thank Department of Science and Technology (DST), India for financial support. The authors thank IPC and CeNSE for characterization facilities, Centre for Earth Science, IISc for ICP-MS analysis and SSCU for DRS and PL facility. The authors are grateful to Prof. Anshu Pandey for TRF facility and Mr. Paresh Samataray for SEM imaging.

View Article Online
DOI: 10.1039/C9NA00305C

References

1. P. K. Samantaray, S. Baloda, G. Madras and S. Bose, *Advanced Sustainable Systems*, 2019, 1800153.
2. C. A. Martínez-Huitle and E. Brillas, *Applied Catalysis B: Environmental*, 2009, **87**, 105-145.
3. N. Rao, A. Dubey, S. Mohanty, P. Khare, R. Jain and S. Kaul, *Journal of hazardous materials*, 2003, **101**, 301-314.
4. P. K. Samantaray, G. Madras and S. Bose, *ChemistrySelect*, 2017, **2**, 7965-7974.
5. P. K. Samantaray, G. Madras and S. Bose, *ACS Sustainable Chemistry & Engineering*, 2018, **7**, 1580-1590.
6. V. Gupta, *Journal of environmental management*, 2009, **90**, 2313-2342.
7. M. R. Gadekar and M. M. Ahammed, *Desalination and Water Treatment*, 2016, **57**, 26392-26400.
8. P. K. Samantaray, G. Madras and S. Bose, *Journal of Membrane Science*, 2018, **548**, 203-214.
9. S. Raghu and C. A. Basha, *Journal of Hazardous Materials*, 2007, **149**, 324-330.
10. S. J. Bhimate, A. D. Kulkarni and A. Tolpadi, *International Journal of Scientific Research & Management Studies*, 2014, 80-87.
11. S. Bose and P. Samantaray, *Proceedings of the Indian National Science Academy*, 2018, **84**, 669-679.
12. J. Chapman, F. Regan and T. Sullivan, *Nanoparticles in anti-microbial materials: Use and characterisation*, Royal Society of Chemistry, 2012.
13. N. Padmavathy, P. K. Samantaray, L. D. Ghosh, G. Madras and S. Bose, *Nanoscale*, 2017, **9**, 12664-12676.
14. J.-M. Herrmann, C. Guillard and P. Pichat, *Catalysis Today*, 1993, **17**, 7-20.
15. A. Fujishima, X. Zhang and D. A. Tryk, *Surface Science Reports*, 2008, **63**, 515-582.
16. P. A. Pekakis, N. P. Xekoukoulotakis and D. Mantzavinos, *Water research*, 2006, **40**, 1276-1286.
17. K. M. Lee, C. W. Lai, K. S. Ngai and J. C. Juan, *Water research*, 2016, **88**, 428-448.
18. A. Fujishima and X. Zhang, *Comptes Rendus Chimie*, 2006, **9**, 750-760.
19. O. Ola and M. M. Maroto-Valer, *Journal of Photochemistry and Photobiology C: Photochemistry Reviews*, 2015, **24**, 16-42.
20. C. Gadiyar, B. Boruah, C. Mascarenhas and V. Shetty, *International. J Curr Eng Tech ISSN*, 2013, 2277-4106.
21. A. G. Prado, L. B. Bolzon, C. P. Pedroso, A. O. Moura and L. L. Costa, *Applied Catalysis B: Environmental*, 2008, **82**, 219-224.
22. A. Mozalev, M. Bendova, R. Vazquez, Z. Pytlicek, E. Llobet and J. Hubalek, *Sensors and Actuators B: Chemical*, 2016, **229**, 587-598.
23. M. Zhang, H. Wen, J. Yu, F. Ai, H. Yu, X. Pan, H. Shao, M. Tang and L. Gai, *Optical Materials Express*, 2017, **7**, 3222-3230.
24. Y. Zhao, C. Ding, Y. Hao, X. Zhai, C. Wang, Y. Li, J. Li and H. Jin, *ACS applied materials & interfaces*, 2018, **10**, 27106-27115.
25. S. Furukawa, T. Shishido, K. Teramura and T. Tanaka, *ChemPhysChem*, 2014, **15**, 2665-2667.
26. X. Chen, T. Yu, X. Fan, H. Zhang, Z. Li, J. Ye and Z. Zou, *Applied Surface Science*, 2007, **253**, 8500-8506.
27. R. Asahi, T. Morikawa, T. Ohwaki, K. Aoki and Y. Taga, *science*, 2001, **293**, 269-271.
28. K. Wilke and H. Breuer, *Journal of Photochemistry and Photobiology A: Chemistry*, 1999, **121**, 49-53.
29. R. Gupta, N. K. Eswar, J. M. Modak and G. Madras, *RSC Advances*, 2016, **6**, 85675-85687.
30. Y. Ma, J. Zhang, B. Tian, F. Chen and L. Wang, *Journal of Hazardous Materials*, 2010, **182**, 386-393.

31. S. Sood, A. Umar, S. K. Mehta, A. Sinha and S. K. Kansal, *Ceramics International*, 2015, **41**, 3533-3540.
32. N. Xinshu, L. Sujuan, C. Huihui and Z. Jianguo, *Journal of rare earths*, 2011, **29**, 225-229.
33. X. Lei, X. Xue and H. Yang, *Applied Surface Science*, 2014, **321**, 396-403.
34. S.-m. Chang and R.-a. Doong, *The Journal of Physical Chemistry B*, 2006, **110**, 20808-20814.
35. D. Falcomer, A. Speghini, G. Ibba, S. Enzo, C. Cannas, A. Musinu and M. Bettinelli, *Journal of Nanomaterials*, 2007, **2007**.
36. A. Esteves, L. C. Oliveira, T. C. Ramalho, M. Goncalves, A. S. Anastacio and H. W. Carvalho, *Catalysis Communications*, 2008, **10**, 330-332.
37. T. Mimani and K. Patil, *Materials Physics and Mechanics(Russia)*, 2001, **4**, 134-137.
38. S. Li, Q. Xu, E. Uchaker, X. Cao and G. Cao, *CrystEngComm*, 2016, **18**, 2532-2540.
39. R. Gupta, B. Boruah, J. M. Modak and G. Madras, *Journal of Photochemistry and Photobiology A: Chemistry*, 2018.
40. V. Morris, R. Farrell, A. Sexton and M. Morris, 2006.
41. S. Ruben, *Handbook of the Elements*, Open Court, 1985.
42. D. P. Dutta, M. Ramakrishnan, M. Roy and A. Kumar, *Journal of Photochemistry and Photobiology A: Chemistry*, 2017, **335**, 102-111.
43. J.-H. Jang, T.-Y. Kim, N.-J. Kim, C.-H. Lee, E.-M. Park, C. Park and S.-J. Suh, *Materials Science and Engineering: B*, 2011, **176**, 1505-1508.
44. A. Naldoni, M. Allieta, S. Santangelo, M. Marelli, F. Fabbri, S. Cappelli, C. L. Bianchi, R. Psaro and V. Dal Santo, *Journal of the American Chemical Society*, 2012, **134**, 7600-7603.
45. S. Stankic, J. Bernardi, O. Diwald and E. Knözinger, *The Journal of Physical Chemistry C*, 2007, **111**, 8069-8074.
46. G. Bhavani, S. Ganesan, S. Selvasekarapandian, S. Monisha and M. Premalatha, *Ionics*, 2016, **22**, 581-592.
47. C. Gionco, M. C. Paganini, E. Giamello, O. Sacco, V. Vaiano and D. Sannino, *Journal of energy chemistry*, 2017, **26**, 270-276.
48. A. Varkey and A. Fort, *Solar Energy Materials and Solar Cells*, 1993, **29**, 253-259.
49. B. Boruah, R. Gupta, J. M. Modak and G. Madras, *Journal of Photochemistry and Photobiology A: Chemistry*, 2019, **373**, 105-115.
50. S. Sathasivam, B. A. Williamson, S. A. Althabaiti, A. Y. Obaid, S. N. Basahel, M. Mokhtar, D. O. Scanlon, C. J. Carmalt and I. P. Parkin, *ACS applied materials & interfaces*, 2017, **9**, 18031-18038.
51. T. El-Shazly, W. M. Hassan, S. T. A. Rahim and N. K. Allam, *international journal of hydrogen energy*, 2015, **40**, 13867-13875.
52. Z. Weibin, W. Weidong, W. Xueming, C. Xinlu, Y. Dawei, S. Changle, P. Liping, W. Yuying and B. Li, *Surface and Interface Analysis*, 2013, **45**, 1206-1210.
53. B. Boruah, R. Gupta, J. M. Modak and G. Madras, *Journal of Photochemistry and Photobiology A: Chemistry*, 2018.
54. S. Farsinezhad, H. Sharma and K. Shankar, *Physical Chemistry Chemical Physics*, 2015, **17**, 29723-29733.
55. Y. Abdollahi, A. Abdullah, Z. Zainal and N. Yusof, *International Journal of Basic & Applied Sciences*, 2011, **11**, 62-69.
56. N. Usha, R. Sivakumar, C. Sanjeeviraja and M. Arivanandhan, *Optik-International Journal for Light and Electron Optics*, 2015, **126**, 1945-1950.
57. V. Agrahari, M. C. Mathpal, M. Kumar and A. Agarwal, *Journal of Alloys and Compounds*, 2015, **622**, 48-53.
58. J. Liqiang, Q. Yichun, W. Baiqi, L. Shudan, J. Baojiang, Y. Libin, F. Wei, F. Honggang and S. Jiazhong, *Solar Energy Materials and Solar Cells*, 2006, **90**, 1773-1787.
59. S. P. Phivilay, A. A. Puretzky, K. Domen and I. E. Wachs, *ACS Catalysis*, 2013, **3**, 2920-2929.

View Article Online
DOI: 10.1039/C9NA00305C

60. A. K. Simlandy, B. Bhattacharyya, A. Pandey and S. Mukherjee, *ACS Catalysis*, 2018, **8**, 5206-5211.
61. N. Sobana, K. Selvam and M. Swaminathan, *Separation and Purification Technology*, 2008, **62**, 648-653.
62. S. Nethaji, A. Sivasamy, G. Thennarasu and S. Saravanan, *Journal of Hazardous Materials*, 2010, **181**, 271-280.
63. R. J. Tayade, T. S. Natarajan and H. C. Bajaj, *Industrial & Engineering Chemistry Research*, 2009, **48**, 10262-10267.
64. Y. Liu, Y. Ohko, R. Zhang, Y. Yang and Z. Zhang, *Journal of hazardous materials*, 2010, **184**, 386-391.
65. A. Gürses, Ç. Doğar, M. Yalçın, M. Açıkyıldız, R. Bayrak and S. Karaca, *Journal of Hazardous Materials*, 2006, **131**, 217-228.
66. L. Zhang, H. Li, Y. Liu, Z. Tian, B. Yang, Z. Sun and S. Yan, *RSC Advances*, 2014, **4**, 48703-48711.
67. R. Godin, Y. Wang, M. A. Zwijnenburg, J. Tang and J. R. Durrant, *Journal of the American Chemical Society*, 2017, **139**, 5216-5224.
68. M. Meetani, M. Rauf, S. Hisaindee, A. Khaleel, A. AlZamly and A. Ahmad, *RSC Advances*, 2011, **1**, 490-497.
69. P. K. Samantaray, S. Baloda, G. Madras and S. Bose, *Journal of Materials Chemistry A*, 2018, **6**, 16664-16679.
70. F. Zhou and Y. Zhu, *Journal of Advanced Ceramics*, 2012, **1**, 72-78.
71. R. Gupta, N. K. Eswar, J. M. Modak and G. Madras, *Catalysis Today*, 2018, **300**, 71-80.
72. R. Georgiev, B. Georgieva, M. Vasileva, P. Ivanov and T. Babeva, *Advances in Condensed Matter Physics*, 2015, **2015**.
73. C.-H. Wu and J.-M. Chern, *Industrial & engineering chemistry research*, 2006, **45**, 6450-6457.